scientific reports

Check for updates

OPEN

Deconvolution of X-ray natural and magnetic circular dichroism in chiral Dy-ferroborate

Daniel Haskel[1]✉, Choongjae Won[2], Yves Joly[3], Jörg Strempfer[1], Gilberto Fabbris[1] & Sang-Wook Cheong[2,4,5]

Structural chirality and magnetism, when intertwined, can have profound implications on materials properties. Using X-ray imaging and spectroscopic measurements that leverage the natural and magnetic circular dichroic effects present in magnetized chiral crystal structures, we probe the interplay between chirality and magnetism across the field-induced spin-flop transition of Dy ferroborate, $DyFe_3(BO_3)_4$. Deconvolution of natural and magnetic circular dichroic signals at the Fe *K* and Dy $L_{2,3}$ absorption edges of the non-centrosymmetric structure was enabled by use of tunable temperature and magnetic field, providing access to element-specific magnetic information across the spin-flop transition. The magnetic response of Fe and Dy sublattices was found to be independent of domain chirality. The chiral domains were robust against both the (chirality preserving) *R32* to $P3_121$/$P3_221$ structural phase transition at 280 K, and application of magnetic field up to 4 Tesla. A third flavor of X-ray dichroism, magneto-chiral dichroism, was not detected within the accuracy of our measurements. The absence of significant Fe magnetization along the screw, *c*-axis for the magnetic field strength used in this study, together with non-linear coupling of magnetic field to electric polarization across the spin-flop transition, may hinder observation of magneto-chiral dichroic effects in this system.

Chirality in matter is fundamental to understanding nature and as a driver of technological advances, from the standard model of particle physics[1] and homochirality of left-handed amino acids as a source of life[2], to strong non-linear optical activity used in laser frequency-doubling[3,4] and new concepts for low-power electronics that leverage electronic band topology[5]. Chiral systems break inversion symmetry (parity odd) and give rise to natural circular dichroism in both optical[6,7] and X-ray regimes[8–10]. X-ray natural circular dichroism (XNCD), the difference in the absorption of X-rays with opposite helicity in chiral systems that preserve time-reversal symmetry, has been measured in a number of crystalline materials[8–14]. While pure electric dipole transitions (E1E1, $\Delta l = +1$ at *K*-edges and $\Delta l = \pm 1$ at $L_{2,3}$ edges) and electric quadrupole transitions (E2E2, $\Delta l = +2$ at *K*-edges and $\Delta l = 0, +2$ at $L_{2,3}$ edges) probe electronic properties that preserve parity, XNCD in chiral systems arises from a non-vanishing E1E2 interference process that is allowed in the presence of parity violation[15–17]. Short X-ray wavelengths in the hard X-ray regime can enhance the E2 contribution in core-level excitations (breakdown of electric dipole approximation, $\mathbf{k} \cdot \mathbf{r} \ll 1$, where k is photon wavenumber and r core electron radius), leading to sizable XNCD signals of order 1%[8–14]. XNCD also provides unique information on orbital hybridization as the E1E2 interference process relies on mixing of otherwise orthogonal valence electronic orbitals by the parity-breaking interaction. For example, XNCD at *K* and L_1 absorption edges (1*s*, 2*s* core level excitation) relies on $p - d$ orbital mixing, while excitations at $L_{2,3}$ absorption edges (2*p* core levels) probe primarily *d*–*f* mixing. Therefore, XNCD in the hard X-ray regime not only detects chiral structural arrangements lacking a center of inversion, but also encodes spectroscopic information on valence band orbital hybridization.

Chiral systems may also display time-reversal symmetry breaking if a non-vanishing (net) magnetization is present alongside chirality. Ferro(ferri)-magnets, "weak" ferromagnets (i.e., antiferromagnets where the Dzyaloshinskii–Moriya interaction originating in spin-orbit coupling induces spin canting and related small spontaneous net magnetization), and canted antiferromagnets in applied magnetic fields, all break time-reversal symmetry. In such systems X-ray magnetic circular dichroism (XMCD) emerges alongside XNCD. The two

[1]Advanced Photon Source, Argonne National Laboratory, Lemont, IL 60439, USA. [2]Laboratory for Pohang Emergent Materials and Max Planck POSTECH Center for Complex Phase Materials, Pohang University of Science and Technology, Pohang 37673, South Korea. [3]Université Grenoble, Institut Néel, F38042 Grenoble, France. [4]Department of Physics and Astronomy, Rutgers, The State University of New Jersey, New Jersey 08854, USA. [5]Keck Center for Quantum Magnetism, Rutgers, The State University of New Jersey, New Jersey 08854, USA. ✉email: haskel@anl.gov

signals can be deconvolved by exploiting their different symmetry properties. The XMCD signal reverses sign upon reversal of magnetization direction relative to the X-ray helicity (photon spin projection along its momentum, $\hbar\mathbf{k}_i$), which can be achieved by either switching the applied magnetic field direction or upon rotation of the magnetized sample by 180° (XMCD $\propto \mathbf{k}_i \cdot \mathbf{m} \propto \cos\theta$)[18,19]. On the other hand, XNCD is independent of the applied magnetic field and when measured with $\mathbf{k}_i \parallel \chi$, where χ is the screw axis along *c*-axis, it is invariant upon 180° rotation of the screw axis relative to the X-ray helicity (angular dependence of E1E2 interference $(3\cos^2\theta - 1)$)[16]. Therefore, while the fidelity of experimental XMCD signals can be evaluated by leveraging the aforementioned sign reversals dictated by the broken time-reversal symmetry, ensuring fidelity of experimental XNCD signals is more challenging. For example, rotation of the screw axis relative to the X-ray helicity over a wide angular range to validate the angular dependence of the E1E2 interference process is challenged in single crystalline samples by contamination ("glitches") from sample Bragg peaks as the X-ray energy is varied across absorption edges. However, a chiral structure and its mirror image form a pair of non-superimposable structures known as enantiomorphs (enantiomers for molecules)[20,21]. In chiral crystals, enantiomorphic domains may be present. The opposite chirality of enantiomorphs leads to a sign reversal of the XNCD signal which can be exploited to ensure signal fidelity, as-long-as enantiomorphs can be measured separately[9,13,14].

The relative magnitude of XNCD and XMCD signals strongly depends on the absorption edge in question. The 1*s*, 2*s* ($l = 0$) core levels excited at *K*- and L_1 edges lack spin-orbit interaction and therefore there is no direct transfer of photon spin angular momentum to spin polarization of the excited electron[18,19]. XMCD at these edges is due to the presence of (weak) spin-orbit coupling in the valence band[22], resulting in typical XMCD signals of order 0.3–1%, which can be significantly smaller than, or comparable to, typical XNCD signals[13]. The situation is reversed at $2p_{\frac{1}{2},\frac{3}{2}}$ (l=1) core levels of $L_{2,3}$ edges where the photon spin generates a sizable spin polarization of the excited electrons[18,19] resulting in larger XMCD than XNCD signals[12].

Simultaneous parity- and time-reversal symmetry breaking can also give rise to X-ray magneto-chiral dichroism (XMχD)[23–25]. This non-reciprocal dichroism is the difference in the absorption of unpolarized X-rays for opposite alignment of incident X-ray wavevector $\mathbf{k}_i$ (along the screw axis) and applied magnetic field direction[12,13,23,26]. XMχD originates in the coupling of local electric fields and atomic magnetic moment so it is intimately connected to linear magneto-electric effects[23–28]. Specifically, XMχD involves the same E1E2 interference terms active in XNCD but combines the orbital toroidal current Ω_z (also known as orbital anapole moment) with the orbital moment, L_z, present in the orbital-mixed ground state. For *K*-edges, the signal is proportional to $\Omega_z(1 - \frac{1}{6}L_z^2)$, and as with XNCD, it reverses sign between enantiomorphs[13,14,23–25].

The Dy ferroborate, $DyFe_3(BO_3)_4$, crystallizes in the *R32* trigonal space group at ambient temperature[29,30], one of the 65 Sohncke space groups for chiral structures[20]. It includes atomic arrangements belonging to right- and left-handed pairs of screw rotations, 3_1, 3_2, with pair components being chiral and non-superimposable mirror images of one another. Right- and left-handed screw chains of FeO_6 octahedra, connected to chains of DyO_6 trigonal prisms, run along the c-axis of the structure, the screw axis[29,30]. A structural transition at $T_s \sim 285$ K transforms the right- and left-handed *R32* structures into corresponding enantiomorphic $P3_121$ and $P3_221$ space group pairs, respectively[29,30]. This transition involves subtle atomic displacements which lower the point symmetry of the Dy ions from *D3* to *C2* and distort both FeO_6 octahedra and DyO_6 trigonal prisms, with changes in Fe–O and Dy–O distances of up to 0.03 Å [29,30]. Magnetically, easy-axis antiferromagnetic ordering with null net magnetization appears below $T_N \sim 38$ K[31]. Compensated Fe spins with low temperature ordered moment of 4.5 μ_B/Fe align with the easy *c*-axis[32]. Compensated Dy spins (6.4 μ_B/Dy) also align primarily along the *c*-axis but develop a small in-plane component below 20 K, likely a result of repopulation of the two lowest lying Dy^{3+} Kramers doublets affecting the magnetic anisotropy of the Dy sublattice[31,32]. Below T_N, a first-order, spin-flop transition can be induced with applied magnetic field along the easy *c*-axis, with critical fields ranging from $H_c \sim 3$ T at low temperature to $H_c \sim 4.5$ T near T_N[31,33]. At the spin-flop transition it was postulated that the Fe spin sublattice flops towards the plane perpendicular to the *c*-axis, while the Dy spin sublattice orients along the applied field and dominates the *c*-axis magnetization[31,33]. A magnetoelectric response is observed across the spin-flop transition, giving rise to *c*-axis electrical polarization values of $P_c \sim 3$ μC/m^2 in the flopped phase at low temperature[34].

Results

We first focus on probing chiral domains and their spectroscopic signatures with XNCD. Figure 1a shows edge-jump normalized XNCD data collected at T = 7 K in zero applied field, with incident X-ray wavevector parallel to the screw *c*-axis (alignment accuracy $\sim 3°$). XNCD is defined as $\mu(\sigma^+) - \mu(\sigma^-)$ where μ is the absorption coefficient obtained from measurements of incident (I_0) and transmitted (I) intensities, μ=ln (I_0/I), and $\sigma^{+,-}$ are opposite helicities of circularly polarized X-rays. The blue and red XNCD spectra were collected with a 50×50 μm^2 beam illuminating two of the three crystal regions marked with X in Fig. 1b, corresponding to the small blue and small red chiral domains shown in Fig. 1c near the bottom edge of the Molybdenum washer supporting the crystal, respectively. As expected, the XNCD signal reverses sign between domains with opposite chirality, although imperfect sign reversal is observed around selected energies due to signal contamination when Bragg reflection conditions are met in the single crystalline sample as the energy is scanned over a wide energy range. Although the XNCD data in Fig. 1a is collected below the magnetic ordering temperature ($T_N \sim$ 38 K), the compensated magnetization of both Fe and Dy sublattices in zero field negates the presence of an XMCD signal. That the XNCD signals are free from XMCD contributions was verified by direct comparison to XNCD data collected at T = 300 K, significantly above T_N (see Supplemental Fig. S1). Since the 2D scanning transmission images shown in Fig. 1c are collected at fixed incident energy (7.799 keV, where the Dy L_3 XNCD signal shows large contrast), edge-step normalization is not possible and chiral contrast in this image is quantified based on the XNCD flipping ratio, i.e., $[\frac{I}{I_0}(\sigma^+) - \frac{I}{I_0}(\sigma^-)]/[\frac{I}{I_0}(\sigma^+) + \frac{I}{I_0}(\sigma^-)]$ (there is an amplitude

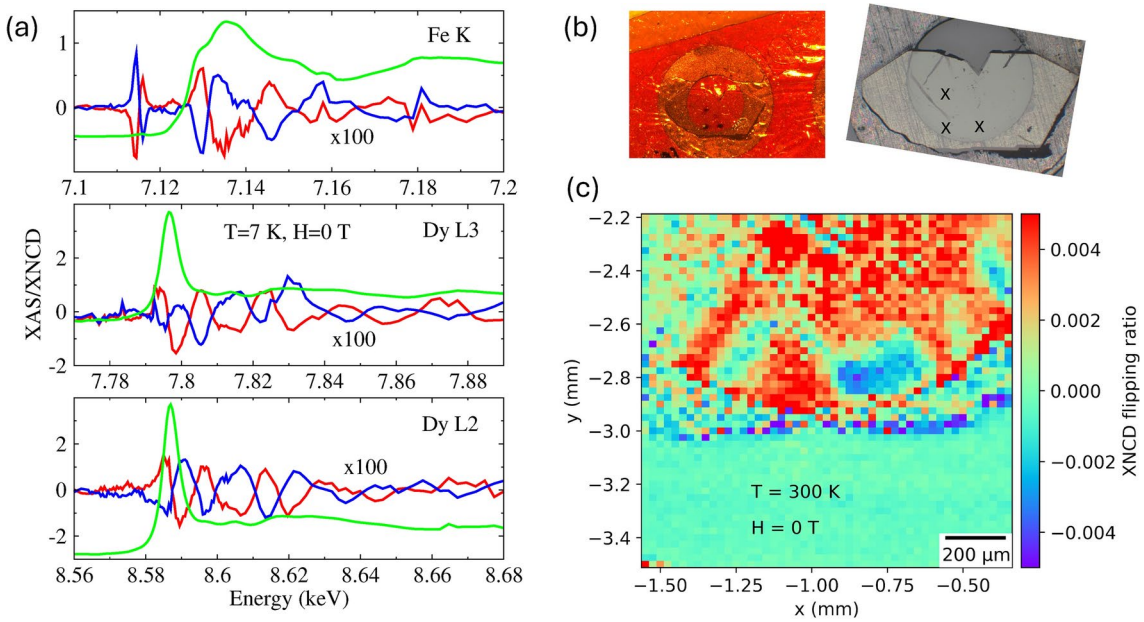

Figure 1. Zero-field XNCD. (**a**) Fe *K* and Dy $L_{2,3}$ X-ray absorption (XAS, green) and XNCD (blue, red) signals collected at T = 7 K in zero applied field. The blue and red XNCD signals were collected on the small blue and small red chiral domains located near the edge of the Mo washer, shown in (**c**), respectively. (**b**) The 28 μm thick single crystalline $DyFe_3(BO_3)_4$ sample used in the transmission measurements mounted on a Mo washer (right), and encapsulated between Kapton foils with a thin layer of vacuum grease for thermal contact (left). The X marks roughly denote illuminated areas, also seen in the left image where black dots from radiation damage of the Kapton layers are visible. The X-ray beam illuminated the crystal from the backside. (**c**) 2D image of chiral domains using XNCD flipping ratio as contrast, collected at T = 300 K in zero applied field using a $50 \times 50 \mu m^2$ X-ray beam with the incident energy tuned to 7.799 keV where the Dy L_3 XNCD signal has a large contrast.

difference as well as a sign inversion between conventional XNCD contrast and its flipping ratio counterpart due to the natural log operation and edge jump normalization in the former). Large XNCD contrast of order 1% is observed at both Fe *K* and Dy $L_{2,3}$ edges. Particularly noteworthy is the large Fe *K*-edge XNCD signal observed below the leading edge where quadrupolar E2 contributions probing empty Fe 3*d* states at the Fermi level are expected to be most significant, despite such contribution being barely visible in the isotropic XAS data. The XNCD signal at the Fe *K*-edge strongly resembles the signal reported for the Sm ferroborate[14]. Also of interest is the same sign of XNCD signal at Dy L_3 and L_2 edges, which contrasts with the sign inversion of XMCD signals across these edges due to the opposite sign of spin-orbit interaction in their respective core levels.

We now add time-reversal symmetry breaking by application of an external magnetic field. An external field of H = 4 T applied along the screw *c*-axis (also the AFM easy axis) at low temperature induces a spin-flop transition leading to a sizable net *c*-axis magnetization, of about 7 μ_B/f.u. (see Supplemental Fig. S2). This net magnetization is believed to arise primarily from the Dy sublattice, while Fe spins align primarily orthogonal to the *c*-axis[31,33].

Figure 2a shows X-ray circular dichroism (XCD) data at T = 7 K measured with opposite field directions (H = ± 4 T) on blue and (small) red chiral domains near the edge of the Mo washer (Fig. 1c). The XCD signals nominally entail a superposition of XNCD and XMCD signals. Visual inspection of XCD signals for opposite applied field direction reveals that the Dy *L*-edge signals are dominated by an XMCD component near absorption threshold (no sign reversal between chiral domains, but sign reversal between opposite applied fields), but have a significant XNCD component above threshold (sign reversal between chiral domains still visible). A 2D image collected at H = 4 T, T = 7 K with incident energy corresponding to peak Dy L_3 XMCD signal (7.796 keV) yields no significant spatial contrast variations confirming that chiral domains are no longer visible due to the dominant XMCD contribution at this energy (see Supplemental Fig. S2). On the other hand, the Fe *K*-edge XCD signal remains largely unchanged upon field reversal implying a negligible XMCD contribution and a dominant XNCD contribution.

The two dichroic responses can be deconvolved by leveraging their different underlying symmetry properties. Subtraction of XCD signals obtained for opposite field directions, followed by division by 2, yields the XMCD signal. Addition yields the XNCD signal. This is done for each chiral domain separately adding redundancy that helps validate the fidelity of the deconvolved signals. Figure 2b shows the deconvolved XMCD and XNCD signals at H = 4 T and T = 7 K. The XMCD signals are the same for both chiral domains at all three absorption edges within the accuracy of the measurements, indicating that the induced magnetization under applied magnetic field is independent of domain chirality. The deconvolved XNCD signals display the expected sign reversal between chiral domains. The good agreement at all three absorption edges between the deconvolved

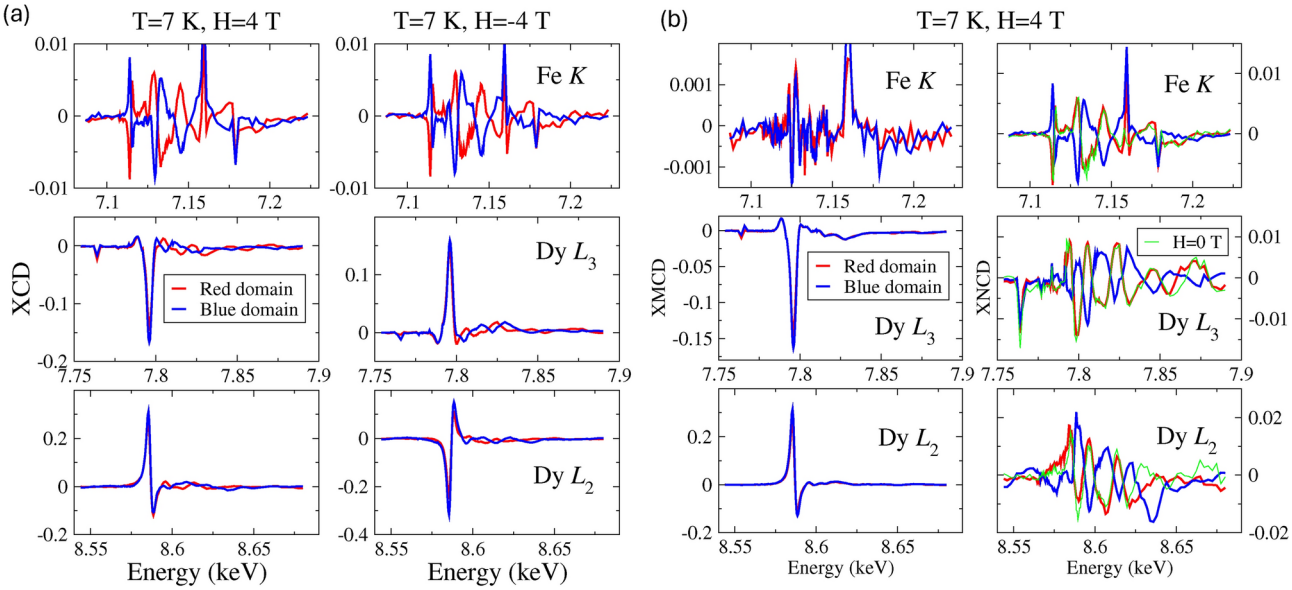

Figure 2. In-field XCD and deconvolution of XMCD and XNCD signals at T=7 K. (**a**) XCD data collected at T = 7 K under application of H = ± 4 T field applied along screw *c*-axis. Blue and red traces correspond to blue and (small) red chiral domains in Fig. 1c. Fe *K*-edge XCD is dominated by XNCD contrast while Dy *L*-edge XCD is dominated by XMCD contrast at threshold but displays visible XNCD contributions above threshold. (**b**) Deconvolution of XNCD and XMCD signals from each chiral domain obtained by addition and subtraction (followed by halving) of XCD data for opposite field directions, respectively. As before, blue and red traces correspond to blue and red chiral domains. The green trace is the XNCD signal from the red chiral domain in the absence of an applied magnetic field.

XNCD signals obtained from the small red chiral domain at H = ± 4 T and T = 7 K, and the XNCD signal obtained from this domain at the same temperature but zero applied field (green trace in Fig. 2b, also shown in Fig. 1a), again confirms that the chiral XNCD signal is independent of the applied magnetic field within the accuracy of the measurement.

Evidence for the robustness of chiral domain structure against both applied magnetic field and the *R32* to $P3_121/P3_221$ structural transition at T_s = 285 K is obtained from 2D XCD images collected at T = 25 K under weaker applied field, H = ± 2 T. The weaker field (below the spin-flop transition) and higher temperature approaching T_N = 38 K results in a roughly 3.5 times smaller induced net magnetization than at 4 T (see Supplemental Fig. S2) preventing XMCD from overwhelming the XCD contrast. Figure 3a,b show 2D images obtained at incident energy E = 7.796 keV where the Dy L_3 XMCD signal shows highest contrast, collected for opposite field directions. Unlike the image collected at 4 T (Supplemental Fig. S2), sizable spatial XCD contrast variations are now observed due to the underlying texture of chiral domains (XNCD signal) superimposed on XMCD contrast. Subtraction and addition of images collected with opposite field directions yields images with XMCD and XNCD contrast, shown in Fig. 3c,d, respectively. Comparison of the XNCD image (T = 25 K, H = 2 T) with that in Fig. 1c (T = 300 K, H = 0 T) shows that the chiral domain structure is preserved across the structural transition at T_s = 285 K and the magnetic ordering transition at T_N = 38 K, as well as in the presence of an applied magnetic field. Although domain walls cannot be resolved with the limited spatial resolution of the measurement (dictated by beam size), the very similar chiral domain pattern and domain sizes in the two images indicates that domain walls did not move under the different temperature and magnetic field conditions used in the measurements. Note that the XNCD image in Fig. 3d covers a larger crystal area than that in Fig. 1c. The X–Y position of the crystal was adjusted to compensate for thermal expansion/contraction of the sample holder to maintain X-ray illumination of chiral domains in the region of interest. The sign inversion of the XNCD contrast in the chiral domains between Figs. 1c and 3d is a result of the former being collected at incident X-ray energy (7.799 keV) which maximizes the XNCD signal, while the latter is collected at 7.796 keV where the XMCD signal is maximized but the XNCD signal inverts sign (see Supplemental Fig. S3).

Discussion

The magnetic structure under applied magnetic field, including within the spin-flop phase, has not been reported and is still unknown. The very large XMCD signals at Dy $L_{2,3}$ edges ($\sim$ 15%) together with a rather small XMCD signal at the Fe *K*-edge (upper limit 0.1%) is consistent with the net magnetization of $\sim 7\mu_B$/f.u. measured at H = 4 T in the spin-flop phase (see Supplemental Fig. S2) arising primarily from the Dy sublattice aligning with the applied magnetic field, as proposed in magnetometry studies, which also postulated that the Fe sublattice aligns mostly orthogonal to the applied magnetic field[31,33]. Neutron diffraction measurements[32] place the magnitude of the Dy ordered moment in zero field at a lower value of $6.4\mu_B$/Dy, so a small Fe contribution to the net magnetization that grows in an applied magnetic field is expected. At H = 4 T, the excess 0.6/3 = 0.2 μ_B/Fe contribution to the magnetization is only 4% of the 4.5 μ_B/Fe ordered moment reported in neutron diffraction

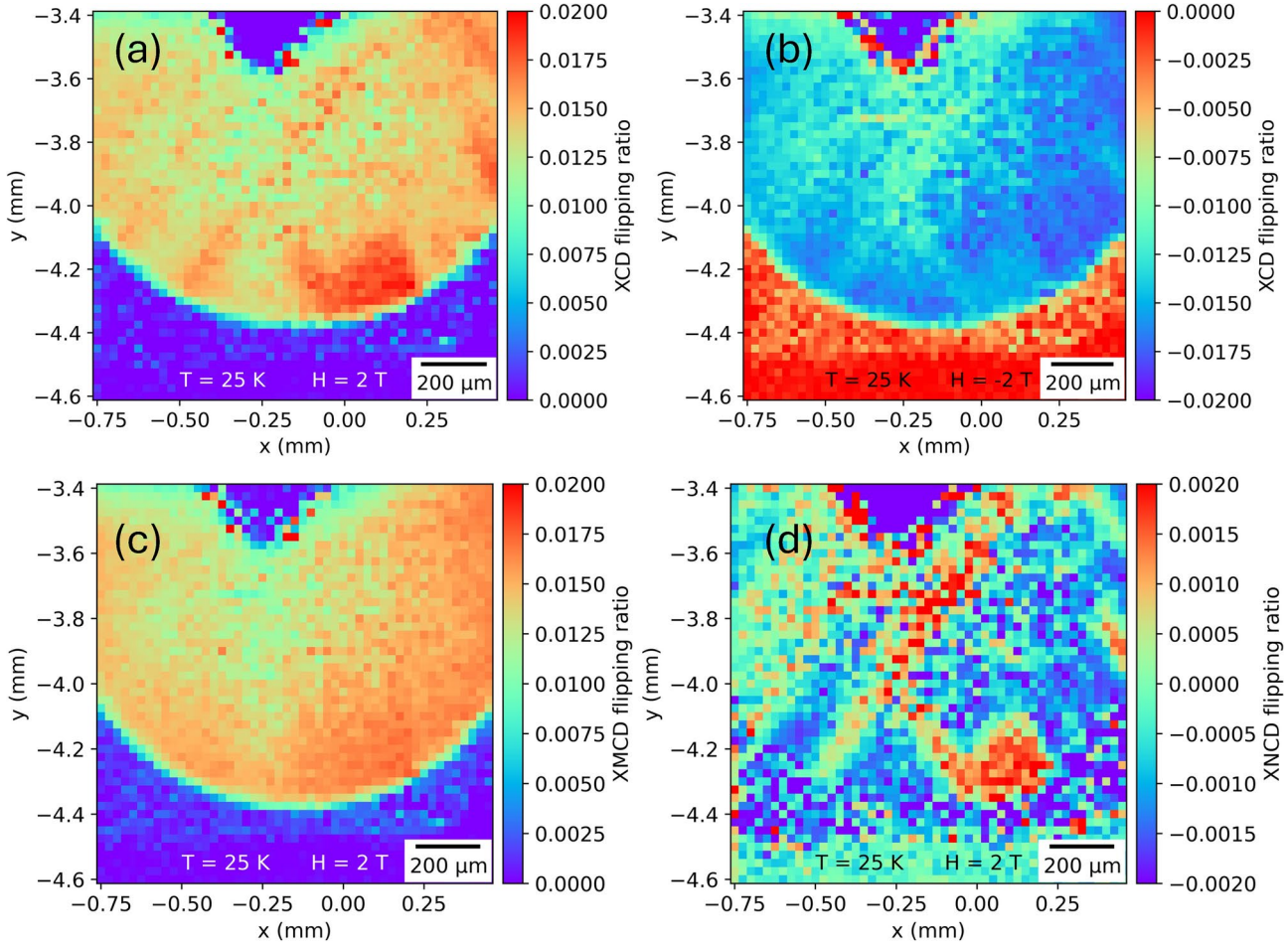

Figure 3. In-field XCD images at the Dy L_3 edge and deconvolution of XMCD and XNCD images, T = 25 K. (**a**, **b**) XCD contrast images collected at T = 25 K and H = ±2 T. Contrast variations are due to chiral texture (XNCD) superimposed on a rather uniform magnetic contrast. (**c**, **d**) XMCD and XNCD images obtained by subtraction and addition of XCD images taken with opposite fields, respectively. The chiral domain structure closely resembles the domain pattern collected at 300 K in zero applied field, shown in Fig. 1c. The sign reversal of blue/red chiral domains between the 25 and 300 K images is due to a sign inversion of the XNCD signal for an incident energy that maximizes the XMCD signal.

measurements[32]. The absence of measurable Fe *K*-edge XMCD signal in the pre-edge region around 7.112 keV, where E1E2 interference leads to a strong XNCD signal (at least 15 times larger than the XMCD signal) is noteworthy. When sizable Fe magnetization is present, this pre-edge region usually displays XMCD signals of about 0.3%, 10 times larger than the noise level. Theoretical simulations of Fe *K*-edge XMCD arising from E1E1 and E2E2 channels in an artificial ferrimagnetic arrangement of Fe moments (see Supplemental Fig. S6) using the FDMNES code[35,36] leads to a 0.4% signal in the pre-edge region. The measured upper limit of 0.05% for the Fe *K*-edge XMCD in the pre-edge region indicates that the Fe sublattice must be aligned mostly orthogonal to the applied magnetic field as expected for spin-flop transitions (XMCD only senses the magnetization component along the X-ray helicity, which is collinear with the applied field). A systematic temperature- and/or field-dependent study of the deconvolved Fe *K*-edge XMCD signal would be required to check if any part of this XMCD signal has a magnetic origin, or if instead it is a result of systematic artifacts due to single crystal Bragg peak contamination at the 0.1% level, even if the signal is the same for both chiral domains (the signal around 7.16 keV is dominated by Bragg peak contamination). We note that, while XMCD sum rules at Dy $M_{4,5}$ and Fe $L_{2,3}$ edges should in principle allow precise determination of the contribution of each sublattice to the net magnetization in applied magnetic field[37,38], XMCD sum rules are not readily applicable at rare-earth $L_{2,3}$ edges due to the intra-atomic 4*f*–5*d* exchange interaction introducing spin-dependence into the radial part of the final state 5*d* orbitals, resulting in helicity-dependent radial dipole matrix elements with the 2*p* core levels[39]. In addition, the *K*-edge sum rule only provides information on the orbital moment of the 4*p* final states[40,41].

That the XNCD signals relate to orbital and not spin degrees of freedom is evident from their sign reversal between enantiomorphic domains, as well as from displaying the same sign (for a given domain) at both L_3 and L_2 edges despite resonant processes at these spin-orbit split core levels generating photoelectrons with opposite spin polarization for a given X-ray helicity[18,19]. The connection between XNCD and the E1E2 interference channel in

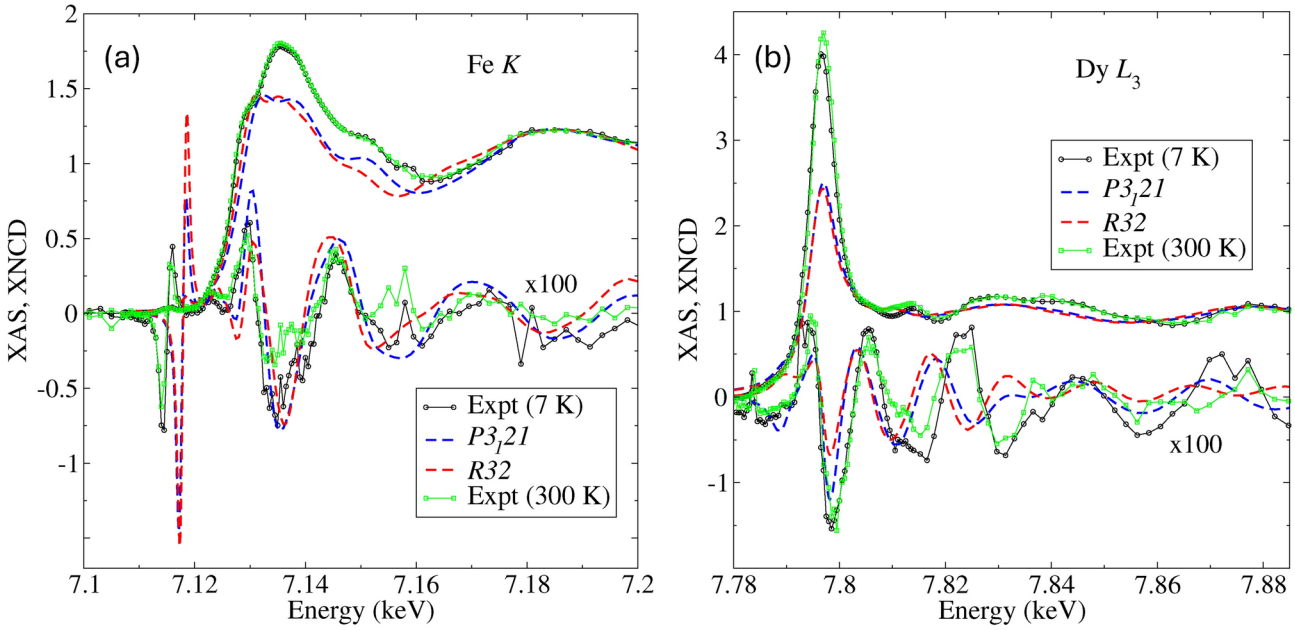

Figure 4. FDMNES simulations of XAS and XNCD spectra. Simulated spectra at (**a**) Fe *K*-edge and (**b**) Dy L_3-edge are shown with dashed lines. The XNCD spectra are computed in the E1E2 interference channel (simulations in E1E1 and E2E2 channels give null XNCD signals, as expected). The experimental data (points) were collected on the small red (7 K) and big red (300 K) chiral domains of Fig. 1c, respectively.

the X-ray absorption cross section is demonstrated by comparison with ab-initio simulations of XNCD spectra using the FDMNES code[35,36], shown in Fig. 4. Simulated spectra are shown for both *R32* and $P3_121$ crystal structures computed using the Finite Difference Method on a 4.5 Å cluster size. The simulations capture some of the main features in the data, although notable disagreements are seen such as in the size and position of the Fe *K* pre-edge XAS and XNCD signals. The simulations show only small changes between the two simulated crystal structures, consistent with the small distortions involved. This is also consistent with a lack of major changes in XNCD data collected below (7 K) and above (300 K) the structural transition (see Supplemental Fig. S1). Additional XNCD measurements at the Dy L_3 edge on a second crystal (not shown) confirm the lack of significant changes in the XNCD signal, as well as the robustness of the chiral domains, between 250 and 300 K (i.e. across the structural transition, see Supplemental Fig. S4). A decomposition of the simulated Dy L_3 XNCD signal into hybridized orbitals (see Supplemental Fig. S5) shows that transitions to *f*–*d* hybridized states dominate the signal, although *p*–*d* and *s*–*f* hybridized states also contribute (E1 transitions are allowed into both 5*d* and 6*s* states, and E2 transitions are allowed into both 4*f* and 6*p* states. At the Fe *K*-edge, only *p*–*d* hybridized states contribute to the XNCD signal). In broad terms, the sensitivity of XNCD to orbital admixtures in chiral structures should be valuable for studies of the interplay between *f* electrons and *s*,*d* conduction electrons in heavy fermions displaying mixed valency and Kondo effects[42,43] as well as the interplay between polarity and chirality in chiral ferroelectrics and multiferroics involving transition metals in ligand coordination where *d*–*p* mixing may be at play[44].

X-ray resonant scattering experiments detected emergence of long-range chiral ordering of both Dy 4*f*[29] and Dy 5*d*[30] quadrupole moments at the *R32* to $P3_121/P3_221$ structural transition. The temperature dependence of these 4*f* and 5*d* quadrupole moments appears to be dictated by the evolution in the population of lowest-lying Kramers doublets in the crystal field split ${}^{S}\mathrm{L}_J = {}^{6}H_{15/2}$ levels, and the influence of distortions in the ligand oxygen atoms, respectively[29,30]. The E1E1 cross section dominating the resonant scattering measurements in Refs. [29,30] probes the parity-even quadrupole component of the pure Dy 4f and 5d charge distribution, while XNCD probes parity-odd components of the admixed (primarily) *f*–*d* states[45]. The lack of significant changes in XNCD between T = 300 K and T = 7 K indicates that the parity-odd components of the admixed charge distribution probed by the E1E2 process do not significantly change across the quadrupole ordering transition. The robustness of chiral domains across the *R32* to $P3_121/P3_221$ structural transition seen here was also observed in the X-ray resonant scattering studies[29].

The simultaneous parity- and time-reversal symmetry breaking that takes place when magnetization is induced with an applied field in this chiral system could give rise to X-ray magneto-chiral dichroism (XMχD), a difference in the absorption of unpolarized X-rays for opposite alignment of incident X-ray wavevector $\mathbf{k}_i$ and applied magnetic field direction[12,13,23–25]. The averaging of X-ray absorption spectra for circularly polarized X-rays with opposite helicities mimics the use of unpolarized X-rays in systems with uniaxial magnetic anisotropy along the screw axis. The difference of such averages between opposite field directions, $[\mu(\sigma^+, H^+) + \mu(\sigma^-, H^+)] - [\mu(\sigma^+, H^-) + \mu(\sigma^-, H^-)]$, allows separating this non-reciprocal dichroism from its natural (XNCD) and magneto-optical (XMCD) counterparts[12,13,23–25]. We were unable to detect a reliable XMχD signal from our measurements in H = ± 4 T fields (like XNCD, XMχD should reverse sign between chiral domains). As noted by Rikken and Raupach[26], a crude

estimate of the strength of XMχD can be obtained from the product of XNCD and XMCD signals, which yields 10^{-5} for the Fe *K*-edge and 1.7×10^{-3} for Dy L_3 edge. Most previous reports of XMχD signals are at *K*-edges of transition metals, where magnetic moments are aligned along the screw axis[12,13,23]. Here, the Fe magnetic moments appear to align mostly orthogonal to the screw axis, resulting in very small if not negligible XMCD signal. Both XMCD and XMχD were shown to scale with net magnetization[13] so, fundamentally, a XMχD signal will be strongly suppressed at the Fe *K*-edge in the field-induced spin-flop phase of Dy ferroborate. Since sizable XMCD and XNCD signals are observed at the Dy *L*-edges, XMχD would be expected if a *linear* magneto-electric effect couples the local electric field to the Dy atomic magnetic moment[23–25]. Although Dy ferroborate displays a magneto-electric response across the spin-flop transition, it was shown[34] that the electric polarization induced by applied field is quadratic rather than linear in applied field, namely, electric polarization does not reverse sign upon reversal of magnetic field direction. This points to magnetostriction as the origin of the induced electric polarization[34]. The absence of a linear coupling between local electric field and magnetic moment may hinder emergence (and detection) of XMχD signal. To the best of our knowledge, there has been only a single report of XMχD at a rare-earth L_3 edge, namely, in the paramagnetic coordination complex holmium oxydiacetate, where the measured XMχD signal of 5×10^{-4} is roughly 10 times smaller than the XNCD signal[12]. We note that, unlike detection of XNCD and XMCD signals, for which the difference in absorption for opposite X-ray helicities is measured at each energy point in a scan and where floor noise level of about 1×10^{-4} is achievable, the superconducting magnet used in our measurements did not allow for fast switching of magnetic field between $+4$ T and -4 T. Since XMχD signals require combination of energy scans for opposite fields collected significantly apart in time, they are much more susceptible to systematic errors making it challenging to detect small XMχD signals at the 1×10^{-4} level, were they to be present. In general, detection schemes where the required high magnetic fields can be rapidly switched alongside X-ray helicity switching at each energy point of an energy scan are desirable for extending the detection limit of weak XMχD signals.

Methods

Crystal growth

Single crystals were grown by $Bi_2Mo_3O_{12}$-B_2O_3 flux methods based on Ref.[46]. Pre-dried Dy_2O_3, Fe_2O_3, B_2O_3, Bi_2O_3, and MoO_3 were mixed and ground in air with a ratio of 30 wt% $DyFe_3(BO_3)_4$ and 70 wt% ($Bi_2Mo_3O_{12}$ + $3B_2O_3$ + 0.5 Dy_2O_3). The mixture was put in a Pt crucible and placed in a SiC box furnace, heated to 1000 °C with a dwelling time of 24 h. Subsequently, the furnace temperature cycled between 965 and 980 °C before the crucible was cooled to 880 °C at a rate of 0.2–0.3 °C per h. To remove the flux, the crucible was removed from the furnace at 880 °C, the flux was poured out, and the $DyFe_3(BO_3)_4$ single crystals were obtained. The remaining flux was eliminated mechanically and etched by diluted nitric acid. The crystals with typical size 1×1 mm^3 were polished to thin platelets with c-axis oriented along surface normal.

Magnetometry and heat capacity

The DC magnetic susceptibility, χ(T), for zero-field cooling was measured over a temperature range of 4–300 K in a magnetic field of 500 Oe. M–H curves at each temperature were obtained in magnetic fields up to 9 T while sweeping the field at a rate of 50 Oe/s. Both magnetic measurements were performed with the magnetic fields oriented along the *c*-axis using a vibrating sample magnetometer. The specific heat was measured on the polished single crystal using a standard relaxation technique. All magnetization and specific heat measurements were conducted in a Quantum Design Dynacool-9T system.

X-ray circular dichroism

X-ray circular dichroism (XCD) measurements at the Fe *K* and Dy $L_{2,3}$ edges were carried out at beamline 4-ID-D of the Advanced Photon Source at Argonne National Laboratory. A pair of toroidal (Pd) and flat (Si) mirrors operated at 3.1 mrad incidence angle were used in combination with detuning of the second crystal in a double crystal monochromator (70% of Bragg peak intensity) to focus the X-ray beam to $\sim 200 \times 200$ μm^2 and reject high energy harmonics. Slits were used to further reduce the beam size to the 50×50 μm^2 beam used in the measurements. A 180 μm thick diamond (111) phase plate operated in Bragg transmission geometry was used to convert the linear X-ray polarization produced by a planar undulator into circularly polarized X-ray beams of either helicity (degree of circular polarization Pc $\sim$ 0.95). XCD measurements were carried out in transmission geometry in polarization switching mode, whereby X-ray helicity is switched at each point in energy scans, or at each sample position in X–Y scans used for 2D imaging of chiral domains at fixed X-ray energy. The 28 μm thick Dy ferroborate single crystal was mounted on a Molybdenum washer and encapsulated between two layers of Kapton foil coated with a very thin layer of Apiezon vacuum grease for thermal contact. The sample was mounted on a Cu holder and inserted into the variable temperature insert of a superconducting cryomagnet providing sample cooling with ^{4}He vapor. The cryomagnet also provided the required magnetic fields collinear with the incident X-ray beam propagation/helicity direction.

FDMNES

Simulations were done using the FDMNES code[35] using the known crystal structures (XNCD) and an arbitrarily chosen ferrimagnetic configuration to induce net magnetization in both Fe and Dy sublattices (XMCD). The ab initio calculations are relativistic with spin-orbit and, in the present paper, realized following Density Functional Theory, known as satisfactory for the *K*-edge of all elements and the $L_{2,3}$ edges of the heavy elements such as Dysprosium. The self-consistent calculations of XNCD presented in this study are performed using either the Finite Difference Method to solve the relativistic Schrödinger equation without any approximation on the potential shape, or the full multiple scattering method. FDMNES works in direct space and the states probed by the photo-electron are calculated in clusters surrounding the different absorbing atoms. The radius R of these clusters are increased up to convergence and we found that in the present case R = 4.5 Å was sufficient.

The calculations account for spectral broadening due to photoelectron self-energy (energy-dependent energy losses) and core-hole lifetime. FDMNES can compute absorption cross sections associated with any incoming photon polarization state (circular or linear). It gives also the contributions of the different transition channels, dipole (E1E1), quadrupole (E2E2) and their interference (E1E2). The last one, important in this paper probes hybridized odd–even states, relevant to XNCD and XMχD signals. The decomposition of XNCD signal into partial contributions from different admixed density of states is computed from the non-diagonal terms of the projection operator, $P(E) = \sum_{\phi} |\phi\rangle\delta(E - E_{\phi})\langle\phi|$. For example, with beam propagating along the screw z axis, K-edge XNCD involves the difference $\langle x|P(E)|yz\rangle - \langle y|P(E)|xz\rangle$ where chirality leads to the symmetry breaking under exchange of x, y coordinates.

Data availability

Raw data can be obtained by contacting Daniel Haskel at haskel@anl.gov.

Received: 21 June 2024; Accepted: 24 September 2024
Published online: 18 October 2024

References

1. Gaillard, M., Grannis, P. D. & Sciulli, F. J. The standard model of particle physics. *Rev. Modern Phys.* **71**, S96–S111 (1999).
2. Blackmond, D. G. *The Origin of Biological Homochirality.*. https://doi.org/10.1101/cshperspect.a032540 (2019).
3. Franke, P. A., Hill, A. E., Peters, C. W. & Weinreich, G. Generation of optical harmonics. *Phys. Rev. Lett.* **7**, 118 (1961).
4. Shadridov, I. V., Zharov, A. A. & Kivshar, Y. S. Second-harmonic generation in nonlinear left-handed metamaterials. *J. Opt. Soc. Am. B* **23**, 529 (2005).
5. Yang, S.-H., Naaman, R., Paltiel, Y. & Parkin, S. S. P. Chiral spintronics. *Nat. Rev. Phys.* **3**, 328–343 (2021).
6. Woody, R. W. Circular dichroism. *Methods Enzymol.* **246**, 34–71 (1995).
7. Miles, A. J., Janes, R. W. & Wallance, B. A. Tools and methods for circular dichroism spectroscopy of proteins: A tutorial review. *Chem. Soc. Rev.* **50**, 8400 (2021).
8. Goulon, J. *et al.* X-ray natural circular dichroism in a uniaxial gyrotropic single crystal of $LiIO_3$. *J. Chem. Phys.* **108**, 6394–6403 (1998).
9. Alagna, L. *et al.* X-ray natural circular dichroism. *Phys. Rev. Lett.* **80**, 4799 (1998).
10. Peacock, R. D. & Stewart, B. Natural circular dichroism in X-ray spectroscopy. *J. Phys. Chem. B* **105**, 351–360 (2001).
11. Goulon, J. *et al.* X-ray natural circular dichroism of gyrotropic crystals. *J. Synchrotron Rad.* **6**, 673–675 (1999).
12. Mitcov, D. *et al.* Hard X-ray magnetochiral dichroism in a paramagnetic molecular 4f complex. *Chem. Sci.* **11**, 8306 (2020).
13. Sessoli, R. *et al.* Strong magneto-chiral dichroism in a paramagnetic molecular helix observed by hard X-rays. *Nat. Phys.* **11**, 69 (2015).
14. Platunov, M. *et al.* X-ray natural circular dichroism imaging of multiferroic crystals. *Crystals* **11**, 531 (2021).
15. Natoli, C. R. *et al.* Calculation of X-ray natural circular dichroism. *Eur. Phys. J. B* **4**, 1–11 (1998).
16. Carra, P. & Benoist, R. X-ray natural circular dichroism. *Phys. Rev. B* **62**, R7703 (2000).
17. Oreshko, A. P., Ovcinnikova, E. N., Kozlovskaya, K. A. & Dmitrienko, V. E. On the calculation of an X-ray natural circular dichroism signal. *Moscow Univ. Phys. Bull.* **73**, 314–324 (2018).
18. Stöhr, J. Exploring the microscopic origin of magnetic anisotropies with X-ray magnetic circular dichroism (XMCD) spectroscopy. *J. Magnet. Magnet. Mater.* **200**, 470–497 (1999).
19. van der Laan, G. & Figueroa, A. I. X-ray magnetic circular dichroism–A versatile tool to study magnetism. *Coordination Chem. Rev.* **277–278**, 95–129 (2014).
20. Fecher, H., Kubler, J. & Felser, C. Chirality in the solid state: Chiral crystal structures in chiral and achiral space groups. *Materials* **15**, 5812 (2022).
21. Zhao, Y. *et al.* Chirality detection of enantiomers using twisted optical metamaterials. *Nat. Commun.* **8**, 14180 (2017).
22. Fano, U. Spin orientation of photoelectrons ejected by circularly polarized light. *Phys. Rev.* **178**, 131 (1969).
23. Goulon, J. *et al.* X-ray magnetochiral dichroism: A new spectroscopic probe of parity nonconserving magnetic solids. *Phys. Rev. Lett.* **88**, 237401 (2002).
24. Di Matteo, S. & Natoli, C. R. Magnetochiral dichroism in Cr_2O_3. *Phys. Rev. B* **66**, 212413 (2002).
25. Di Matteo, S. & Natoli, C. R. Erratum: Magnetochiral dichroism in Cr_2O_3. *Phys. Rev. B.* **72**, 139901(E) (2005).
26. Rikken, G. L. J. A. & Raupach, E. Observation of magneto-chiral dichroism. *Nature* **390**, 493 (1997).
27. Di Matteo, S., Joly, Y. & Natoli, C. R. Detection of electromagnetic multipoles by X-ray spectroscopies. *Phys. Rev. B* **72**, 144406 (2005).
28. Lovesey, S. W. & Balcar, E. Quantum theory of natural circular, magneto-chiral and non-reciprocal linear dichroism. *Phys. Scr.* **81**, 065703 (2010).
29. Usui, T. *et al.* Observation of quadrupole helix chirality and its domain structure in $DyFe_3(BO_3)_4$. *Nat. Mater.* **13**, 611 (2014).
30. Nakajima, H. *et al.* Quadrupole moments in chiral material $DyFe_3(BO_3)_4$ observed by resonant X-ray diffraction. *Phys. Rev. B* **93**, 144116 (2016).
31. Popova, E. A. *et al.* Magnetization and specific heat of $DyFe_3(BO_3)_4$ single crystal. *Eur. Phys. J. B* **62**, 123–128 (2008).
32. Ritter, C., Pankrats, A., Gudim, I. & Vorotynov, A. Magnetic structure of iron borate $DyFe_3(BO_3)_4$: A neutron diffraction study. *J. Phys. Conf. Series* **340**, 012065 (2012).
33. Volkov, D. V., Demidov, A. A. & Kolmakova, N. P. Magnetic properties of $DyFe_3(BO_3)_4$. *JETP* **106**, 723–730 (2008).
34. Popov, Y. F. *et al.* Observation of spontaneous spin reorientation in $Nd_{1-x}Dy_xFe_3(BO_3)_4$ ferroborates with a competitive R-Fe exchange. *JETP Lett.* **89**, 345–351 (2009).
35. Joly, Y. X-ray absorption near-edge structure calculations beyond the muffin-tin approximation. *Phys. Rev. B* **63**, 125120 (2001).
36. Joly, Y. *et al.* Self-consistency, spin-orbit and other advances in the FDMNES code to simulate XANES and RXD experiments. *J. Phys. Conf. Ser.* **190**, 012007 (2009).
37. Carra, P., Thole, B. T., Altarelli, M. & Wang, X. X-ray circular dichroism and local magnetic fields. *Phys. Rev. Lett.* **70**, 694 (1993).
38. Chen, C. T. *et al.* Experimental confirmation of the X-ray magnetic circular dichroism sum rules for iron and cobalt. *Phys. Rev. Lett.* **75**, 152 (1995).
39. van Veenendaal, M., Goedkoop, J. B. & Thole, B. T. Branching ratios of the circular dichroism at rare earth $L_{2,3}$ edges. *Phys. Rev. Lett.* **78**, 1162 (1997).
40. Thole, B. T., Carra, P., Sette, F. & van der Laan, G. X-ray circular dichroism as a probe of orbital magnetization. *Phys. Rev. Lett.* **68**, 1943 (1992).
41. Guo, G. Y. What does the K-edge X-ray magnetic circular dichroism spectrum tell us?. *J. Phys. Condens. Matter.* **8**, L747–L752 (1996).
42. Ota, Y. *et al.* Pressure effect on the chiral helimagnetic order in $YbNi_3Al_9$. *J. Phys. Soc. Jpn.* **89**, 044715 (2020).

43. Ohara, S. *et al.* Study of chiral structure and magnetism in heavy-fermion $Yb(Ni_{1-x}Cu_x)_3Al_9$. *JPS Conf. Proc.* **3**, 017016 (2014).
44. Zheng, H. *et al.* Chiral multiferroicity in two-dimensional hybrid organic-inorganic perovskites. *Nat. Commun.* **15**, 5556 (2024).
45. Lovesey, S. W., Balcar, E., Knight, K. S. & Fernández Rodriguez, J. Electronic properties of crystalline materials observed in X-ray diffraction. *Phys. Rep.* **411**, 233–289 (2005).
46. Gudim, A. I. *et al.* Single-crystal growth of trigonal $DyFe_3(BO_3)_4$ and study of magnetic properties. *Crystallogr. Rep.* **53**, 1140–1143 (2008).

Acknowledgements
We thank Jong-Woo Kim for helpful discussions. Work at Argonne was supported by the U.S. DOE Office of Science, Office of Basic Energy Sciences, under Award No. DE-AC0206CH11357. C.W. and SWC were supported by the National Research Foundation of Korea (NRF) funded by the Ministry of Science and ICT (No. 2022M3H4A1A04074153). SWC was partially supported by the W. M. Keck foundation Grant to the Keck Center for Quantum Magnetism at Rutgers University.

Author contributions
D.H. and S.-W.C. conceived the project. C. W. synthesized the crystals and carried out magnetometry and heat capacity measurements. D.H., J.S. and G.F. carried out X-ray measurements. Y. J. carried out FDMNES simulations. D.H. wrote the manuscript with input from all authors.

Declarations

Competing interests
The authors declare no competing interests.

Additional information
Supplementary Information The online version contains supplementary material available at https://doi.org/10.1038/s41598-024-74111-2.

Correspondence and requests for materials should be addressed to D.H.

Reprints and permissions information is available at www.nature.com/reprints.

Publisher's note Springer Nature remains neutral with regard to jurisdictional claims in published maps and institutional affiliations.